Propagating spin waves in nanometer-thick yttrium iron garnet films: Dependence on wave vector, magnetic field strength, and angle

Huajun Qin,* Sampo J. Hämäläinen, Kristian Arjas, Jorn Witteveen, and Sebastiaan van Dijken†
NanoSpin, Department of Applied Physics, Aalto University School of Science, P.O. Box 15100, FI-00076 Aalto, Finland

(Received 22 August 2018; revised manuscript received 7 November 2018; published 26 December 2018)

We present a comprehensive investigation of propagating spin waves in nanometer-thick yttrium iron garnet (YIG) films. We use broadband spin-wave spectroscopy with integrated coplanar waveguides (CPWs) and antennas on top of continuous and patterned YIG films to characterize spin waves with wave vectors up to 10 rad/μm. All films are grown by pulsed laser deposition. From spin-wave transmission spectra, parameters such as the Gilbert damping constant, spin-wave dispersion relation, group velocity, relaxation time, and decay length are derived, and their dependence on magnetic bias field strength and angle is systematically gauged. For a 40-nm-thick YIG film, we obtain a damping constant of 3.5×10^{-4} and a maximum decay length of 1.2 mm. We show a strong variation of spin-wave parameters with wave vector, magnetic field strength, and field angle. The properties of spin waves with small wave vectors change considerably with in-plane magnetic bias field up to 30 mT and magnetic field angle beyond 20°. We also compare broadband spin-wave spectroscopy measurements on 35-nm-thick YIG films with integrated CPWs and antennas and demonstrate that both methods provide similar spin-wave parameters.

DOI: 10.1103/PhysRevB.98.224422

I. INTRODUCTION

Magnonics aims at the exploitation of spin waves for information transport, storage, and processing [1–7]. For practical devices, it is essential that spin waves propagate over long distances in thin films. Because of its ultralow damping constant, ferrimagnetic yttrium iron garnet (YIG) is a promising material. Bulk crystals and micrometer-thick YIG films exhibit a Gilbert damping constant $\alpha \approx 3 \times 10^{-5}$ at gigahertz frequencies. In recent years, nanometer-thick YIG films with ultralow damping have been prepared successfully. High-quality YIG films have been grown on $Gd_3Ga_5O_{12}$ (GGG) single-crystal substrates using liquid-phase epitaxy [8–12], magnetron sputtering [13–17], and pulsed laser deposition (PLD) [18–28]. For these YIG films, damping parameters with values approaching those of bulk crystals have been reported [13,18,24]. Meanwhile, YIG-based magnonic devices such as logic gates, transistors, and multiplexers have been demonstrated [29–33]. Spin-wave transmission in nanometer-thick YIG films [34–40] and the excitation of short-wavelength spin waves have also been investigated [41–45]. In experiments on spin-wave propagation [34–43], the properties of Damon-Eshbach spin waves with k perpendicular to the direction of in-plane magnetization are commonly assessed, and consequently, a comprehensive study on the evolution of spin-wave parameters in YIG films upon field rotation is lacking. In addition, all-electrical spectroscopy methods often rely on the use of coplanar waveguides (CPWs), and effects of antenna geometry on the extraction of spin-wave properties is not well established.

In this paper, we present a broadband spin-wave spectroscopy study of PLD-grown YIG films with thicknesses of 35 and 40 nm. Spin-wave transmission spectra are recorded by patterning CPWs and antennas on top of continuous and patterned YIG films. CPWs are used because they generate spin waves with well-defined wave vectors. This enables extraction of key parameters such as the Gilbert damping constant α, spin-wave dispersion relation, group velocity υ_g, relaxation time τ, and decay length l_d. For a 40-nm YIG film, we find $\alpha \approx 3.5 \times 10^{-4}$ and a maximum group velocity and decay length of 3.0 km/s and 1.2 mm, respectively. We show how the properties of spin waves vary as a function of the in-plane magnetic bias field strength and angle. We find particularly strong tuning of spin-wave parameters if $k < 4.5$ rad/μm and the magnetic bias field ranges from 0 to 30 mT. Strong effects are also attained by rotating a constant magnetic field more than $\phi_H = 20°$ away from the Damon-Eshbach geometry. From a detailed comparison of spin-wave transmission spectra recorded with two CPWs or two antennas, we conclude that both measurement methods result in the extraction of similar spin-wave parameters.

This paper is organized as follows. In Sec. II, we describe the PLD process, broadband spin-wave spectroscopy setup, and simulations of the CPW and antenna excitation spectra. In Sec. III, we present vector network analyzer ferromagnetic resonance (VNA-FMR) results and broadband spin-wave transmission spectra for CPWs. In Sec. IV, we fit the experimental data and extract parameters of propagating spin waves. Spin-wave transmission measurements using CPWs and antennas are also compared. Section V summarizes the paper.

*huajun.qin@aalto.fi
†sebastiaan.van.dijken@aalto.fi

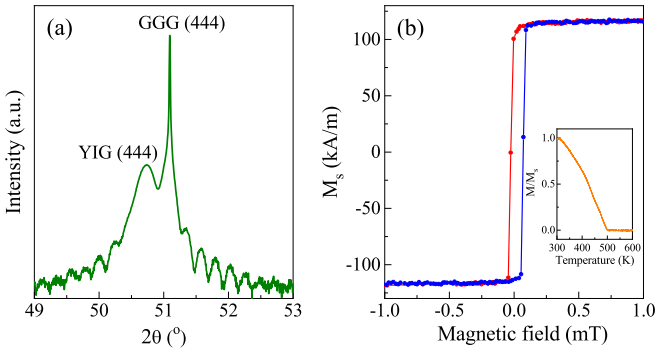

FIG. 1. (a) XRD θ-2θ scan of the (444) reflections from a PLD-grown YIG film on a GGG(111) substrate. The period of Laue oscillations surrounding the (444) peaks corresponds to a film thickness of 40 nm. (b) Room-temperature VSM hysteresis loop of the same film. The inset shows how the YIG saturation magnetization varies with temperature.

II. EXPERIMENT

A. PLD of YIG thin films

YIG films with thicknesses of 35 and 40 nm were grown on single-crystal GGG(111) substrates using PLD. Prior to loading into the PLD vacuum chamber, the substrates were ultrasonically cleaned in acetone, isopropanol, and deionized water. The substrates were first degassed at 550 °C for 15 min and then heated to 800 °C at a rate of 5 °C per minute in an O_2 pressure of 0.13 mbar. YIG films were deposited under these conditions by ablation from a stoichiometric target using an excimer laser with a pulse repetition rate of 2 Hz and a fluence of 1.8 J/cm^2. After deposition, the YIG films were first annealed at 730 °C for 10 min in 13 mbar O_2 before cooling down to room temperature at a rate of −3 °C per minute.

B. Structural and magnetic characterization

The crystal structure of our YIG films was inspected by high-resolution x-ray diffraction (XRD) on a Rigaku SmartLab system. Figure 1(a) shows an XRD θ-2θ scan of a 40-nm-thick YIG film on GGG(111). Clear (444) film and substrate peaks are surrounded by Laue oscillations, signifying epitaxial and smooth film growth. We used a vibrating sample magnetometer (VSM) in a Dynacool physical property measurement system from Quantum Design to characterize the magnetic properties. Figure 1(b) depicts a VSM hysteresis loop of a 40-nm-thick YIG film. At room temperature, the coercive field of the YIG film is only 0.1 mT, and the saturation magnetization M_s is 115 kA/m. The evolution of M_s with temperature is shown in the inset of Fig. 1(b). From these data, we derive a Curie temperature T_C of around 500 K. The values of M_s and T_C are similar to those obtained in previous studies on nanometer-thick YIG films [15,18,25] and about 10% smaller than values of YIG bulk crystals (M_s = 139 kA/m, T_C = 559 K). Minor off stoichiometries in the YIG film might be the reason for the small discrepancy [46].

C. Broadband spin-wave spectroscopy

VNA-FMR and spin-wave transmission measurements were performed using a two-port VNA and a microwave probing station with a quadrupole electromagnet. In VNA-FMR experiments, the YIG film was placed face-down onto a prepatterned CPW on a GaAs substrate, as shown in Fig. 2(a). The signal line and ground lines of this CPW had widths of 50 and 800 μm, respectively, and were separated by 30 μm.

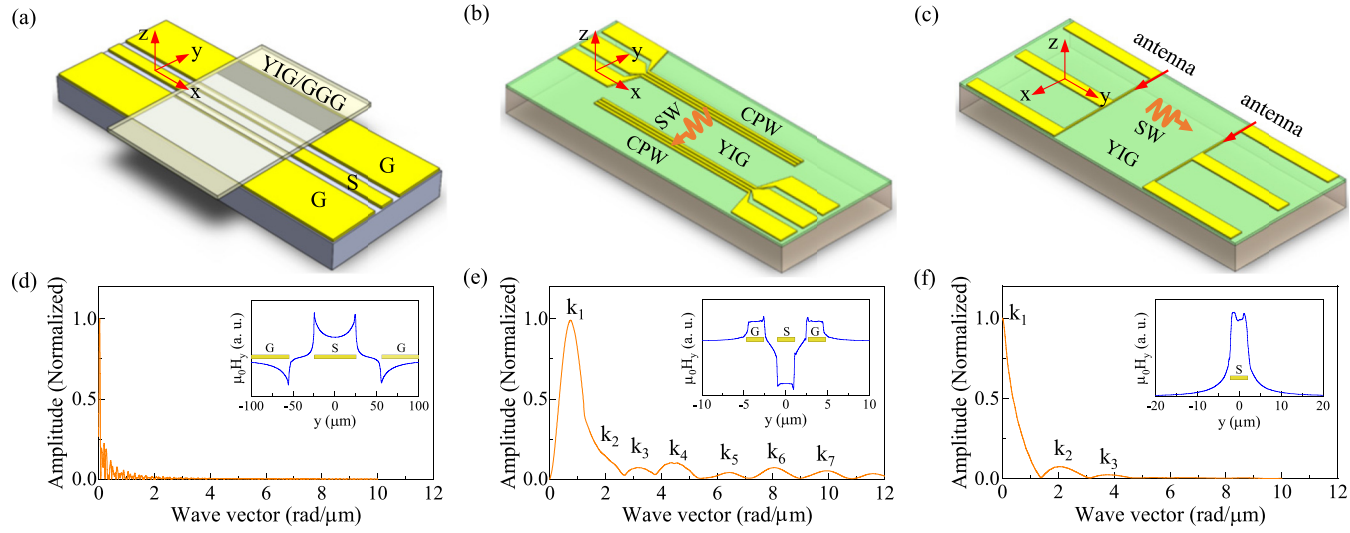

FIG. 2. (a)–(c) Schematic illustrations of several measurement configurations used in this study. (a) VNA-FMR measurements are performed by placing the YIG/GGG sample facedown onto a CPW. The CPW consists of a 50-μm-wide signal line and two 800-μm-wide ground lines. The gap between the signal and ground lines is 30 μm. Transmission of spin waves (SW) through the YIG film is characterized by patterning (b) two CPWs or (c) two antennas on top of a YIG film. The signal and ground lines of the CPWs in (b) are 2 μm wide and separated by 1.6-μm gaps. The antennas, which are marked by red arrows in (c), are 4 μm wide. (d)–(f) Simulated spin-wave excitation spectra of the different antenna structures. The in-plane rf magnetic fields $\mu_0 h_y^{rf}$ that are produced by passing a microwave current through the CPWs in (a) and (b) or the antenna in (c) are shown in the insets.

Broadband spin-wave spectroscopy in transmission geometry was conducted by contacting two integrated CPWs or antennas on top of a continuous YIG film or YIG waveguide, as shown in Figs. 2(b) and 2(c). Most of the experiments were performed with CPWs consisting of 2-μm-wide signal and ground lines with a separation of 1.6 μm. For comparison measurements, we used CPWs and antennas with 4-μm-wide signal lines. All antenna structures were fabricated by photolithography and consisted of 3 nm of Ta and 120 nm of Au. A microwave current provided by a VNA was used to generate a rf magnetic field around one of the CPWs or antennas. We used CST MICROWAVE STUDIO software to simulate the excitation spectra of the antenna structures (see next section).

Spin waves that are excited by a rf magnetic field produce an inductive voltage across a nearby antenna. At the exciting CPW or antenna, this voltage is given by [47]

$$V_{\text{ind}} \propto \int \chi(\omega, k)|\rho(k)|^2 dk, \tag{1}$$

where $\chi(\omega, k)$ is the magnetic susceptibility and $|\rho(k)|^2$ is the spin-wave excitation spectrum. Propagating spin waves arriving at the receiving CPW or antenna produce an inductive voltage:

$$V_{\text{ind}} \propto \int \chi(\omega, k)|\rho(k)|^2 \exp[-i(ks + \Phi_0)]dk, \tag{2}$$

where s is the propagation distance and Φ_0 is the initial phase of the spin waves. In our experiments, we used the first port of the VNA to measure these inductive voltages by recording the S_{12} scattering parameter.

D. Simulations of CPW and antenna excitation spectra

We used CST MICROWAVE STUDIO software to simulate the spin-wave excitation spectra of the different antenna structures [48]. This commercial solver of Maxwell's equations uses a finite integration method to calculate the rf magnetic field $\mu_0 h^{rf}$ and its in-plane ($\mu_0 h_x^{rf}$, $\mu_0 h_y^{rf}$) and out-of-plane ($\mu_0 h_z^{rf}$) components. Since the excitation field along the CPW or antenna $\mu_0 h_x^{rf}$ is nearly uniform and $\mu_0 h_z^{rf}$ is much smaller than $\mu_0 h_y^{rf}$, we Fourier transformed only the latter component. Figure 2 depicts the CPW and antenna configurations used in the experiments together with their simulated spin-wave excitation spectra. The large prepatterned CPW on a GaAs substrate [Fig. 2(a)], which we used for VNA-FMR measurements, mainly excites spin waves with $k \approx 0$ rad/μm [Fig. 2(d)]. The excitation spectrum of the smaller integrated CPW with a 2-μm-wide signal line [Fig. 2(b)] includes one main spin-wave mode with wave vector $k_1 = 0.76$ rad/μm and several high-order modes, k_2–k_7 [Fig. 2(e)]. The 4-μm-wide antenna [Fig. 2(c)] mainly excites spin waves with k_1 ranging from 0 to 1.5 rad/μm and some higher-order modes at $k_2 \approx 2.0$ rad/μm and $k_3 \approx 3.8$ rad/μm [Fig. 2(f)]. The insets of Figs. 2(d)–2(f) show the simulated rf magnetic fields $\mu_0 h_y^{rf}$ along the y axis for each antenna structure.

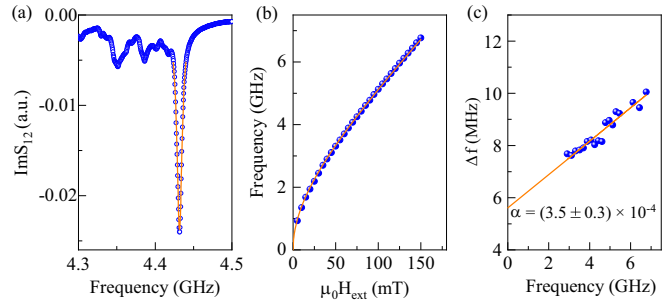

FIG. 3. (a) Imaginary part of the S_{12} scattering parameter showing FMR for an in-plane external magnetic bias field of 80 mT along the CPW. The orange line is a Lorentzian function fit. (b) FMR frequency as a function of external magnetic bias field. The orange line represents a fit to the experimental data using the Kittel formula. (c) Dependence of the FMR linewidth Δf on resonance frequency. From a linear fit to the data, we derive $\alpha = (3.5 \pm 0.3) \times 10^{-4}$.

III. RESULTS

A. VNA-FMR

We recorded FMR spectra for various in-plane external magnetic bias fields by measuring the S_{12} scattering parameter on a 40-nm-thick YIG film. As an example, the imaginary part of S_{12} recorded with a magnetic bias field $\mu_0 H_{\text{ext}} = 80$ mT is shown in Fig. 3(a). The plotted spectrum was obtained by subtracting a reference measurement recorded at a bias field of 200 mT to remove a background signal. The prominent peak at $f = 4.432$ GHz corresponds to the YIG FMR mode. It is well fitted by a Lorentzian function, indicated by the orange line. From similar data taken at other bias fields, we extracted the field dependence of FMR frequency and the evolution of the resonance linewidth Δf with frequency. Figures 3(b) and 3(c) summarize our results. Fitting the data of Fig. 3(b) to the Kittel formula $f_{\text{res}} = \frac{\gamma\mu_0}{2\pi}\sqrt{H_{\text{ext}}(H_{\text{ext}} + M_{\text{eff}})}$, we find $M_{\text{eff}} = 184 \pm 3$ kA/m and $\gamma/2\pi = 28.08$ GHz/T. The latter value corresponds to $g = 2.006$. The measured value of M_{eff} is comparable to those of other PLD-grown YIG films [23,25,26,37], but it is large compared to M_s (115 kA/m). Since $M_{\text{eff}} = M_s - H_{\text{ani}}$, the anisotropy field $H_{\text{ani}} = -69$ kA/m in our film. This negative anisotropy field is caused by a lattice mismatch between the YIG film and GGG substrate [25]. Fitting the data of Fig. 3(c) using $\Delta f = 2\alpha f + v_g \Delta k$ gives a Gilbert damping constant $\alpha = (3.5 \pm 0.3) \times 10^{-4}$ and an intercept $v_g \Delta k$ of 5.6 MHz. In this formula, v_g and Δk are the spin-wave group velocity and excitation-spectrum width [49]. The Gilbert damping constant of our YIG films is comparable to other experimental data on PLD-grown YIG films, which are typically in the 10^{-4} range [20–27]. Small differences in α may be due to imperfect crystallinity or off stoichiometry of YIG films caused by oxygen vacancies [25,26] or ion diffusion from the substrate [28].

B. Propagating spin waves

We measured spin-wave transmission spectra on a 40-nm-thick YIG film. In these experiments, we used photolithography and argon ion-beam milling to fabricate YIG waveguides with 45° edges to reduce spin-wave interference, as illustrated

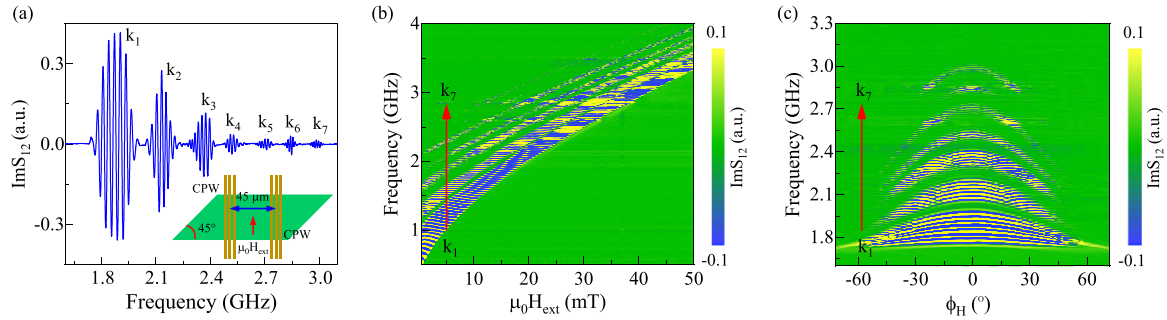

FIG. 4. (a) Spin-wave transmission spectrum (imaginary part of S_{12}) recorded on a 40-nm-thick YIG waveguide with an external magnetic bias field $\mu_0 H_{\text{ext}} = 15.5$ mT along the CPWs. The inset shows a top-view schematic of the Damon-Eshbach measurement geometry. (b) Two-dimensional map of spin-wave transmission spectra measured as a function of magnetic bias field strength. (c) Angular dependence of spin-wave transmission spectra for a constant bias field of 15.5 mT. The field angle $\phi_H = 0^\circ$ corresponds to the Damon-Eshbach configuration.

in the inset of Fig. 4(a). On top of the waveguides, two parallel CPWs for spin-wave excitation and detection were patterned. The CPW parameters were identical to those in Fig. 2(b), and their signal lines were separated by 45 μm. During broadband spin-wave spectroscopy, spin waves with characteristic wave vectors k_i $(i = 1, 2, \dots)$ were excited by passing a rf current through one of the CPWs. After propagation through the YIG film, the other CPW inductively detected the spin waves. Figure 4(a) shows the imaginary part of the S_{12} scattering parameter for an external magnetic bias field $\mu_0 H_{\text{ext}} = 15.5$ mT parallel to the CPWs (Damon-Eshbach configuration). The graph contains seven envelope-type peaks (k_1–k_7) with clear periodic oscillations. The peak intensities decrease with frequency because of reductions in the excitation efficiency and spin-wave decay length. The oscillations signify spin-wave propagation between the CPWs [49]. Figure 4(b) shows a two-dimensional representation of spin-wave transmission spectra recorded at different bias fields. As the field strengthens, the frequency gaps between spin-wave modes become smaller. Figure 4(c) depicts the angular dependence of S_{12} spectra at a constant magnetic bias field of 15.5 mT. In this measurement, the in-plane magnetic bias field was rotated from -72° to 72°, where $\phi_H = 0^\circ$ corresponds to the Damon-Eshbach configuration. As the magnetization rotates towards the wave vector of propagating spin waves, the frequency and intensity of the k_1–k_7 modes drop. The frequency evolutions of the spin-wave modes in Figs. 4(b) and 4(c) are explained by a flattening of the dispersion relation with increasing magnetic bias field strength and angle.

IV. DISCUSSION

A. Fitting of spin-wave transmission spectra

We used Eq. (2) to fit spin-wave transmission spectra. In this equation, $\chi(\omega, k)$ is described by a Lorentzian function, while the excitation spectrum $|\rho(k)|^2$ is approximated by a Gaussian function [see Fig. 2(e)]. For Damon-Eshbach spin waves with $kd \ll 1$, the wave vector is given by $k = \frac{2}{d}\frac{f^2 - f_{\text{res}}^2}{(\gamma\mu_0 M_{\text{eff}}/2\pi)^2}$, where d is the film thickness. Based on these approximations, we write Eq. (2) as

$$\text{Im}S_{12} \propto \frac{\Delta f}{(f - f_{\text{res}})^2 + (\Delta f)^2} e^{-4\ln 2(k-k_i)^2/\Delta k^2} \times \sin(ks + \Phi_0), \tag{3}$$

where Δf is the S_{12} envelope width, Δk is the width of the spin-wave excitation spectrum, Φ_0 is the initial phase, and s is the propagation distance. Figure 5 shows a fitting result for a spin-wave transmission spectrum with $\mu_0 H_{\text{ext}} = 15.5$ mT and $\phi_H = 0^\circ$. As input parameters, we used $f_{\text{res}} = 1.75$ GHz, $d = 40$ nm, $s = 45$ μm, and $M_{\text{eff}} = 184$ kA/m, which are either determined by geometry or extracted from measurements. Δf, Δk, and k_i are fitting parameters. For the k_1 peak, we obtained the best fit for $\Delta f = 0.25$ GHz, $\Delta k = 0.6$ rad/μm, and $k_1 = 0.72$ rad/μm. The k_2 peak was fitted with $k_2 = 1.87$ rad/μm. The values of Δk and k_i are in good agreement with the simulated excitation spectrum of the CPW [Fig. 2(e)], and Δf matches the width of the envelope peak in the experimental S_{12} spectrum.

B. Spin-wave dispersion relations

We extracted spin-wave dispersion relations for different magnetic bias fields and field angles by fitting the S_{12} transmission spectra shown in Figs. 4(b) and 4(c). The symbols in Fig. 6 summarize the results. We also calculated the dispersion relations using the Kalinikos and Slavin formula [50]:

$$f = \frac{\gamma\mu_0}{2\pi}\left(H_{\text{ext}}\left\{H_{\text{ext}} + M_{\text{eff}}\left[1 - P\sin^2\phi_H + \frac{M_{\text{eff}}}{H_{\text{ext}}}P(1-P)\cos^2\phi_H\right]\right\}\right)^{1/2}, \tag{4}$$

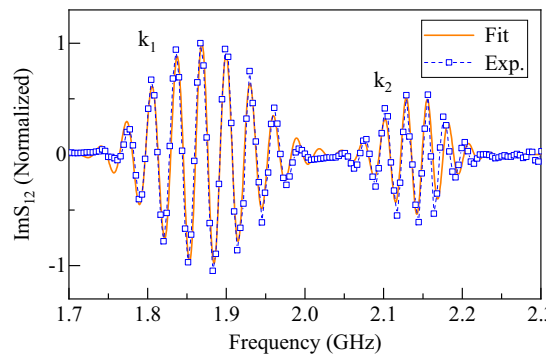

FIG. 5. Fit to the spin-wave transmission spectrum for $\mu_0 H_{\text{ext}} = 15.5$ mT and $\phi_H = 0^\circ$ (blue squares) using Eq. (3) (orange line).

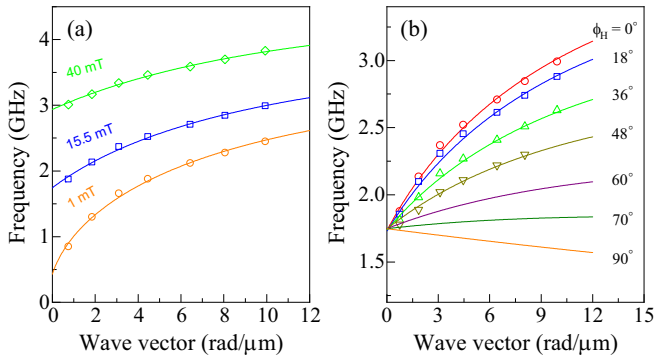

FIG. 6. Spin-wave dispersion relations for (a) different external magnetic bias fields and (b) field angles. In (a) $\phi_H = 0\,^\circ$, and in (b) $\mu_0 H_{\text{ext}} = 15.5$ mT. The colored lines represent fits to the dispersion relations using Eq. (4).

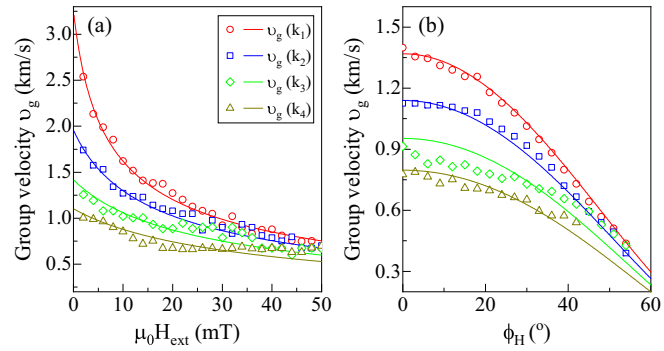

FIG. 7. Spin-wave group velocity υ_g of k_1–k_4 modes as a function of (a) external magnetic bias field and (b) field angle. In (a) $\phi_H = 0\,^\circ$, and in (b) $\mu_0 H_{\text{ext}} = 15.5$ mT. The symbols and colored lines represent experimentally derived values and calculations using Eq. (6).

with $P = 1 - \frac{1-e^{-kd}}{kd}$. The calculated dispersion relations for $\gamma/2\pi = 28.08$ GHz/T, $M_{\text{eff}} = 184$ kA/m, and $d = 40$ nm are shown as lines in Fig. 6. The dispersion curves flatten with increasing magnetic bias field. For instance, at $\mu_0 H_{\text{ext}} = 1$ mT, the frequency of propagating spin waves changes from 0.5 to 2.4 GHz for wave vectors ranging from 0 to 10 rad/μm. At $\mu_0 H_{\text{ext}} = 40$ mT, the evolution of frequency with wave vector is reduced to 3–3.7 GHz. This magnetic-field dependence of the dispersion relation narrows the spin-wave transmission bands in Fig. 4(b) at large $\mu_0 H_{\text{ext}}$.

The angular dependence of the spin-wave dispersion curves in Fig. 6(b) is explained by in-plane magnetization rotation from $M \perp k$ ($\phi_H = 0\,^\circ$) towards $M \parallel k$ ($\phi_H = 90\,^\circ$). At $\phi_H = 0\,^\circ$, dispersive Damon-Eshbach spin waves with positive group velocity propagate between the CPWs. The character of excited spin waves changes gradually with increasing ϕ_H until it has fully transformed into a backward-volume magnetostatic mode at $\phi_H = 90\,^\circ$. This mode is only weakly dispersive and exhibits a negative group velocity.

C. Group velocity

The phase relation between signals from the two CPWs is given by $\Phi = ks$ [49]. Since the phase shift between two neighboring maxima δf in broadband spin-wave transmission spectra corresponds to 2π, the group velocity can be written as

$$\upsilon_g = \frac{\partial\omega}{\partial k} \approx \frac{2\pi\delta f}{2\pi/s} = \delta f s, \tag{5}$$

where $s = 45$ μm in our experiments. Using this equation, we extracted the spin-wave group velocity for wave vectors k_1–k_4 from the transmission spectra shown in Figs. 4(b) and 4(c). Figure 7 summarizes the variation of υ_g with external magnetic bias field and field angle. For weak bias fields ($\mu_0 H_{\text{ext}} < 30$ mT), the group velocity decreases swiftly, especially for k_1 and k_2. For instance, $\upsilon_g(k_1)$ reduces from 3.0 to 1.0 km/s in the 0–30 mT field range, while $\upsilon_g(k_3)$ changes only from 1.2 to 0.8 km/s. At larger external magnetic bias fields ($\mu_0 H_{\text{ext}} > 30$ mT), υ_g decreases more slowly for wave vectors k_1–k_4. Figure 7(b) shows how υ_g varies as a function of field angle at $\mu_0 H_{\text{ext}} = 15.5$ mT. For all wave vectors, the group velocity is largest in the Damon-Eshbach configuration ($\phi_H = 0°$). At larger field angles, υ_g decreases, and its dependence on wave vector diminishes. Variations of the spin-wave group velocity with wave vector and magnetic-field strength or angle are explained by a flattening of the dispersion relations, as illustrated by the data in Fig. 6.

From Eq. (4), we derived an expression for the spin-wave group velocity:

$$\begin{aligned}\upsilon_g &= 2\pi\,\partial f/\partial k \\ &= \left(\frac{\gamma\mu_0}{2\pi}\right)^2 \frac{\pi}{f}\left\{H_{\text{ext}} M_{\text{eff}}\left[-P'\sin^2\phi_H\right.\right. \\ &\quad \left.\left. + \frac{M_{\text{eff}}}{H_{\text{ext}}}(1-2P)P'\cos^2\phi_H\right]\right\},\end{aligned} \tag{6}$$

where $P' = \frac{(1-e^{-kd}-kde^{-kd})d}{(kd)^2}$. Using $\gamma/2\pi = 28.08$ GHz/T, $M_{\text{eff}} = 184$ kA/m, and $d = 40$ nm as input parameters, we calculated υ_g for wave vectors k_1–k_4 as a function of external magnetic bias field and field angle. The results are shown as colored lines in Figs. 7(a) and 7(b). The model calculations and experimentally derived data for υ_g agree well.

D. Spin-wave relaxation time and decay length

We now discuss the relaxation time τ and decay length l_d of spin waves in our YIG films. Following Ref. [51], the relaxation time is estimated by $\tau = 1/2\pi\alpha f$. Using $\alpha = 3.5 \times 10^{-4}$ and spin-wave transmission data from Fig. 4, we determined τ for wave vectors k_1–k_4. The experimental dependence of τ on the external magnetic bias field and field angle is shown in Fig. 8 together with calculations based on the spin-wave dispersion relation [Eq. (4)]. We note that we obtain good agreement between the experimentally derived data and calculations by assuming a single value of the Gilbert damping parameter. The maximum spin-wave relaxation time in our 40-nm-thick YIG films is approximately 500 ns. Resembling the spin-wave group velocity, τ is largest for small wave vectors, and it decreases with increasing bias field [Fig. 8(a)]. In contrast to υ_g, the spin-wave relaxation time is smallest in the Damon-Eshbach configuration ($\phi_H = 0°$), and it evolves more strongly with increasing ϕ_H if k is large [Fig. 8(b)]. This result is explained by $\tau \propto 1/f$ and a

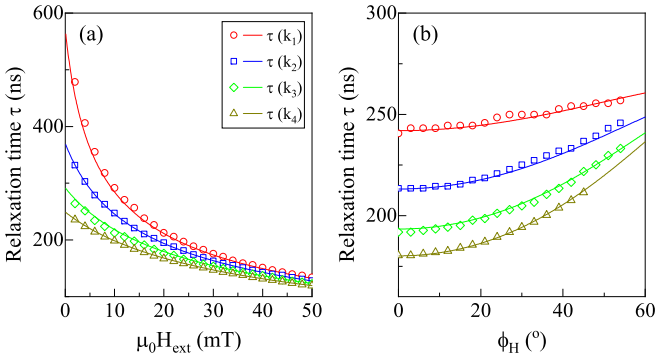

FIG. 8. Experimentally derived (symbols) and calculated values (lines) of the spin-wave relaxation time τ of k_1–k_4 modes as a function of (a) external magnetic bias field and (b) field angle. In (a) $\phi_H = 0\,^\circ$, and in (b) $\mu_0 H_{\text{ext}} = 15.5$ mT.

lowering of the spin-wave frequency if the in-plane bias field rotates the magnetization towards k [see Fig. 4(c)].

The spin-wave decay length is derived using $l_d = \upsilon_g \times \tau$ with the experimental and calculated curves of Figs. 7 and 8 as input. Figure 9(a) shows the dependence of l_d on $\mu_0 H_{\text{ext}}$ for wave vectors k_1–k_4. The largest spin-wave decay length in our 40-nm-thick YIG films is 1.2 mm, which we measured for $k_1 = 0.72$ rad/μm and $\mu_0 H_{\text{ext}} = 2$ mT. The decay length decreases with magnetic bias field to about 100 μm at $\mu_0 H_{\text{ext}} = 50$ mT. Figure 9(b) depicts the dependence of l_d on the direction of a 15.5-mT bias field. The spin-wave decay length decreases substantially with ϕ_H for small k, but its angular dependence weakens for larger wave vectors.

The decay of propagating spin waves between the exciting and detecting CPWs in broadband spectroscopy measurements is given by $\exp(-s/l_d)$ [51]. Based on the results of Fig. 9, one would thus expect the intensity of spin waves to drop with increasing wave vector and in-plane bias field strength or angle. The spin-wave transmission spectra of Fig. 4 confirm this behavior.

The decay lengths of spin waves in our YIG films compare well to previously published results. Since other studies on YIG films exclusively focused on Damon-Eshbach spin waves, we compare data for this geometry. The decay length,

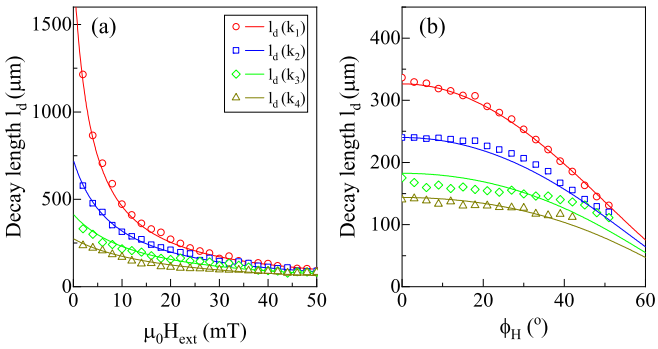

FIG. 9. Experimentally derived (symbols) and calculated values (lines) of the spin-wave decay length l_d of k_1–k_4 modes as a function of (a) external magnetic bias field and (b) field angle. In (a) $\phi_H = 0\,^\circ$, and in (b) $\mu_0 H_{\text{ext}} = 15.5$ mT.

$l_d = \upsilon_g/2\pi\alpha f$, is largest for spin waves with high group velocity and small magnetic damping or frequency. Yu *et al.* measured a decay length $l_d = 580$ μm in a 20-nm-tick YIG film at a frequency $f = 1.1$ GHz and magnetic bias field $\mu_0 H_{\text{ext}} = 5$ mT [34]. At a higher frequency of 3 GHz, Collet *et al.* measured $l_d = 25$ μm for $\mu_0 H_{\text{ext}} = 45$ mT in a film of the same thickness [36], and Talalaevskij *et al.* recorded a value $l_d = 2.7$ μm on a 38-nm-thick YIG film at $f = 6$ GHz and $\mu_0 H_{\text{ext}} = 160$ mT [38]. Much larger spin-wave decay lengths are commonly found for thicker films because of smaller damping and higher group velocities. For example, in a 200-nm-thick YIG film with $\alpha = 1.0 \times 10^{-4}$ and $\upsilon_g = 2.5$ km/s, a decay length $l_d = 2.2$ mm was measured at $f = 1.78$ GHz and $\mu_0 H_{\text{ext}} = 20$ mT [39]. In our 40-nm-thick YIG films, we measured a maximum l_d of 1.2 mm at $f = 0.97$ GHz and $\mu_0 H_{\text{ext}} = 2$ mT. Large decay lengths like this are essential for the implementation of YIG-based thin-film devices.

E. CPWs versus antennas

Finally, we compare broadband spin-wave spectroscopy measurements on YIG films using CPWs and antennas. In these experiments, the CPW and antenna structures had 4-μm-wide signal lines, and they were patterned onto the same 35-nm-thick YIG film. For comparison, we also recorded transmission spectra on 50-μm-wide YIG waveguides. The separation distance s between the CPWs or antennas was set to 110 or 220 μm. Schematics of the different measurement geometries are depicted on the sides of Fig. 10. Transmission spectra that were obtained for Damon-Eshbach spin waves in each configuration are also shown. In all measurements, we used an in-plane external magnetic bias field of 10 mT. The plots focus on phase oscillations in the first-order excitation at k_1 (higher-order excitations were also measured but are not shown). The differently shaped outlines of the S_{12} peak for two CPWs (left) or two antennas (right) mimic the profiles of their excitation spectra (Fig. 2). As expected from $\delta f = \upsilon_g/s$, the period of frequency oscillations δf becomes smaller if the separation between CPWs or antennas s is enlarged [Figs. 10(c) and 10(f)].

We fitted the spin-wave transmission spectra obtained with CPWs [Figs. 10(a)–10(c)] using the same procedure as described earlier. Good agreements between experimental data (squares) and calculations (orange lines) were obtained by inserting $M_{\text{eff}} = 190 \pm 5$ kA/m, $\Delta f = 0.18 \pm 0.03$ GHz, $k = 0.34 \pm 0.02$ rad/μm, and $\Delta k = 0.33 \pm 0.03$ rad/μm into Eq. (3). To fit S_{12} spectra measured by antennas, we approximated the wave vector of the excitation as $k = \frac{2}{d}\frac{f^2 - f_{\text{res}}^2}{(\gamma\mu_0 M_{\text{eff}}/2\pi)^2} H(f - f_{\text{res}})$, where H is a Heaviside step function [52]. The best results were achieved for $M_{\text{eff}} = 178 \pm 5$ kA/m, $\Delta f = 0.25 \pm 0.05$ GHz, $k = 0$ rad/μm, and $\Delta k = 0.65 \pm 0.05$ rad/μm. From this data comparison, we conclude that broadband spin-wave spectroscopy measurements with CPWs and antennas yield similar results for M_{eff}. We also note that the S_{12} peak width Δf obtained from measurements on continuous YIG films and YIG waveguides are nearly identical ($\Delta f = 0.18$ GHz for CPWs, $\Delta f = 0.22$ GHz for antennas). Patterning of the YIG film into waveguides therefore does not deteriorate the Gilbert damping constant.

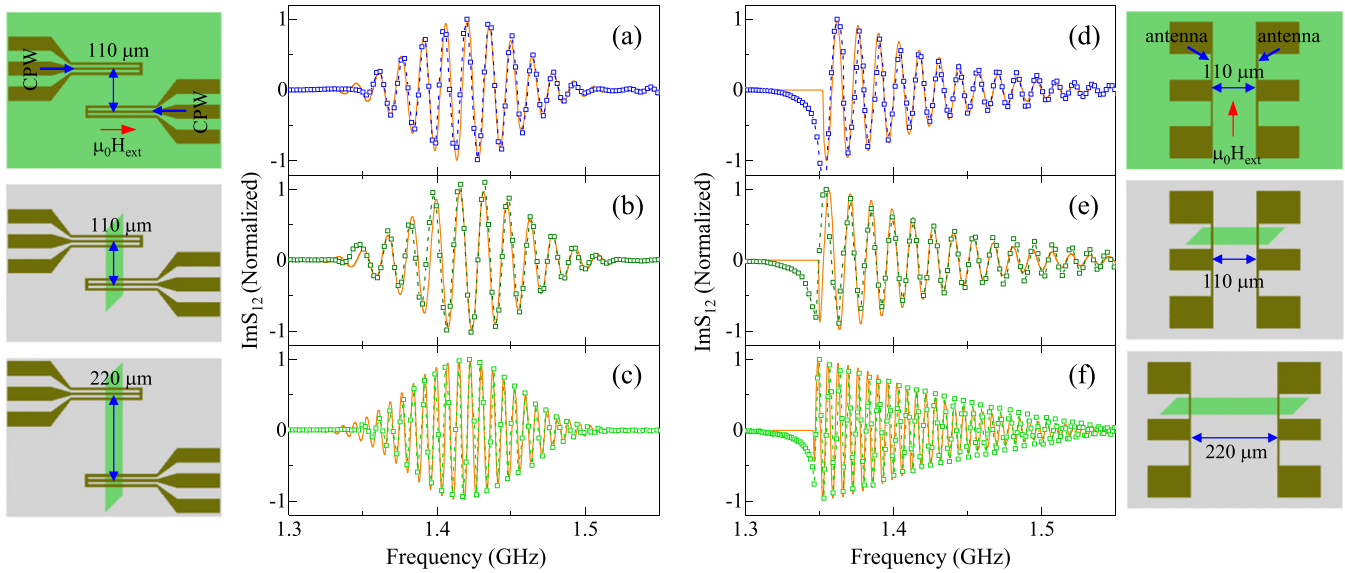

FIG. 10. Spin-wave transmission spectra measured using CPWs on (a) a continuous YIG film and (b) and (c) 50-μm-wide YIG waveguides. The YIG film and waveguides are 35 nm thick, and the CPWs are separated by 110 μm in (a) and (b) and 220 μm in (c). (d)–(f) Spin-wave transmission spectra measured using antennas on the same YIG film and waveguides. The signal lines of the CPWs and antennas are 4 μm wide. The orange lines represent fits to the experimental data using Eq. (3). The measurement geometry for each spectrum is illustrated next to the graphs. In the schematics, green and gray areas depict the YIG film or waveguide and GGG substrate, respectively.

From the oscillation periods δf in the transmission spectra of Fig. 10, we extracted the properties of propagating spin waves. Here we take spin waves with $f = 1.42$ GHz as an example. By averaging δf over the same frequency range in CPW- and antenna-measured spectra, we obtained $\upsilon_g = 1.62 \pm 0.03$ km/s and $\upsilon_g = 1.53 \pm 0.04$ km/s, respectively. For the spin-wave relaxation time we found $\tau = 1/2\pi\alpha f = 225$ ns for both measurement configurations, and the extracted decay lengths were $l_d = 365 \pm 7$ μm (CPW) and $l_d = 344 \pm 9$ μm (antenna). These data demonstrate that broadband spin-wave spectroscopy measurements on YIG films with CPWs or antennas provide comparable results. The small differences in the derived values of υ_g and l_d are caused by the distinctive shapes of the spin-wave excitation spectra for the two antenna structures.

V. SUMMARY

In conclusion, we prepared nanometer-thick epitaxial YIG films with a Gilbert damping constant $\alpha = 3.5 \times 10^{-4}$ on GGG(111) substrates using PLD. The dependence of spin-wave transmission on the strength and angle of an in-plane magnetic bias field was systematically gauged. We demonstrated strong tuning of the spin-wave group velocity υ_g, relaxation time τ, and decay length l_d up to a field strength of 30 mT and beyond a field angle of 20°. In the 0–30-mT field range, υ_g and l_d of Damon-Eshbach spin waves with $k_1 = 0.72$ rad/μm changed from 3 km/s and 1.2 mm to 1 km/s and 0.15 mm, respectively. For a constant field of 15.5 mT, the group velocity and spin-wave decay length depended strongly on k if $\phi_H = 0°$–$20°$. Strong tuning of these parameters at larger field angles diminished their variation with wave vector. Our experimental observations are reproduced by calculations based on the Kalinikos and Slavin model. Moreover, we showed that broadband spin-wave spectroscopy performed with integrated CPWs and antennas gives similar spin-wave parameters.

ACKNOWLEDGMENTS

This work was supported by the European Research Council (Grants No. ERC-2012-StG 307502-E-CONTROL and No. ERC-PoC-2018 812841-POWERSPIN) and the Academy of Finland (Grants No. 317918 and No. 320021). S.J.H. acknowledges financial support from the Väisälä Foundation. Lithography was performed at the Micronova Nanofabrication Centre, supported by Aalto University. We also acknowledge the computational resources provided by the Aalto Science-IT project.

[1] A. A. Serga, A. V. Chumak, and B. Hillebrands, J. Phys. D **43**, 264002 (2010).
[2] V. V. Kruglyak, S. O. Demokritov, and D. Grundler, J. Phys. D **43**, 264001 (2010).
[3] B. Lenk, H. Ulrichs, F. Garbs, and M. Mnzenberg, Phys. Rep. **507**, 107 (2011).
[4] M. Krawczyk and D. Grundler, J. Phys.: Condens. Matter **26**, 123202 (2014).
[5] A. V. Chumak, V. I. Vasyuchka, A. A. Serga, and B. Hillebrands, Nat. Phys. **11**, 453 (2015).
[6] S. A. Nikitov, D. V. Kalyabin, I. V. Lisenkov, A. Slavin, Y. N. Barabanenkov, S. A. Osokin, A. V. Sadovnikov, E. N. Beginin, M. A. Morozova, Y. A. Filimonov *et al.*, Phys. Usp. **58**, 1002 (2015).
[7] A. V. Chumak, A. A. Serga, and B. Hillebrands, J. Phys. D **50**, 244001 (2017).

[8] C. Hahn, G. de Loubens, O. Klein, M. Viret, V. V. Naletov, and J. Ben Youssef, Phys. Rev. B **87**, 174417 (2013).

[9] P. Pirro, T. Brächer, A. V. Chumak, B. Lägel, C. Dubs, O. Surzhenko, P. Görnert, B. Leven, and B. Hillebrands, Appl. Phys. Lett. **104**, 012402 (2014).

[10] G. Wang, H. Liu, H. Wu, X. Li, H. Qiu, Y. Yang, B. Qu, T.-L. Ren, X. Han, R. Zhang *et al.*, Appl. Phys. Lett. **109**, 162405 (2016).

[11] C. Dubs, O. Surzhenko, R. Linke, A. Danilewsky, U. Brückner, and J. Dellith, J. Phys. D **50**, 204005 (2017).

[12] N. Beaulieu, N. Kervarec, N. Thiery, O. Klein, V. Naletov, H. Hurdequint, G. de Loubens, J. B. Youssef, and N. Vukadinovic, IEEE Magn. Lett. **9**, 1 (2018).

[13] H. Chang, P. Li, W. Zhang, T. Liu, A. Hoffmann, L. Deng, and M. Wu, IEEE Magn. Lett. **5**, 1 (2014).

[14] J. Lustikova, Y. Shiomi, Z. Qiu, T. Kikkawa, R. Iguchi, K. Uchida, and E. Saitoh, J. Appl. Phys. **116**, 153902 (2014).

[15] J. C. Gallagher, A. S. Yang, J. T. Brangham, B. D. Esser, S. P. White, M. R. Page, K.-Y. Meng, S. Yu, R. Adur, W. Ruane *et al.*, Appl. Phys. Lett. **109**, 072401 (2016).

[16] A. Mitra, O. Cespedes, Q. Ramasse, M. Ali, S. Marmion, M. Ward, R. M. D. Brydson, C. J. Kinane, J. F. K. Cooper, S. Langridge *et al.*, Sci. Rep. **7**, 11774 (2017).

[17] P. Cao Van, S. Surabhi, V. Dongquoc, R. Kuchi, S.-G. Yoon, and J.-R. Jeong, Appl. Surf. Sci. **435**, 377 (2018).

[18] C. Hauser, T. Richter, N. Homonnay, C. Eisenschmidt, M. Qaid, H. Deniz, D. Hesse, M. Sawicki, S. G. Ebbinghaus, and G. Schmidt, Sci. Rep. **6**, 20827 (2016).

[19] B. Heinrich, C. Burrowes, E. Montoya, B. Kardasz, E. Girt, Y.-Y. Song, Y. Sun, and M. Wu, Phys. Rev. Lett. **107**, 066604 (2011).

[20] Y. Sun, Y.-Y. Song, H. Chang, M. Kabatek, M. Jantz, W. Schneider, M. Wu, H. Schultheiss, and A. Hoffmann, Appl. Phys. Lett. **101**, 152405 (2012).

[21] O. d'Allivy Kelly, A. Anane, R. Bernard, J. Ben Youssef, C. Hahn, A. H. Molpeceres, C. Carrétéro, E. Jacquet, C. Deranlot, P. Bortolotti *et al.*, Appl. Phys. Lett. **103**, 082408 (2013).

[22] M. C. Onbasli, A. Kehlberger, D. H. Kim, G. Jakob, M. Kläui, A. V. Chumak, B. Hillebrands, and C. A. Ross, APL Mater. **2**, 106102 (2014).

[23] B. M. Howe, S. Emori, H. M. Jeon, T. M. Oxholm, J. G. Jones, K. Mahalingam, Y. Zhuang, N. X. Sun, and G. J. Brown, IEEE Magn. Lett. **6**, 1 (2015).

[24] L. V. Lutsev, A. M. Korovin, V. E. Bursian, S. V. Gastev, V. V. Fedorov, S. M. Suturin, and N. S. Sokolov, Appl. Phys. Lett. **108**, 182402 (2016).

[25] N. S. Sokolov, V. V. Fedorov, A. M. Korovin, S. M. Suturin, D. A. Baranov, S. V. Gastev, B. B. Krichevtsov, K. Y. Maksimova, A. I. Grunin, V. E. Bursian *et al.*, J. Appl. Phys. **119**, 023903 (2016).

[26] B. Bhoi, B. Kim, Y. Kim, M.-K. Kim, J.-H. Lee, and S.-K. Kim, J. Appl. Phys. **123**, 203902 (2018).

[27] T. Yoshimoto, T. Goto, K. Shimada, B. Iwamoto, Y. Nakamura, H. Uchida, C. A. Ross, and M. Inoue, Adv. Electron. Mater. **4**, 1800106 (2018).

[28] S. M. Suturin, A. M. Korovin, V. E. Bursian, L. V. Lutsev, V. Bourobina, N. L. Yakovlev, M. Montecchi, L. Pasquali, V. Ukleev, A. Vorobiev *et al.*, Phys. Rev. Mater. **2**, 104404 (2018).

[29] T. Schneider, A. A. Serga, B. Leven, B. Hillebrands, R. L. Stamps, and M. P. Kostylev, Appl. Phys. Lett. **92**, 022505 (2008).

[30] K. Ganzhorn, S. Klingler, T. Wimmer, S. Geprägs, R. Gross, H. Huebl, and S. T. B. Goennenwein, Appl. Phys. Lett. **109**, 022405 (2016).

[31] T. Fischer, M. Kewenig, D. A. Bozhko, A. A. Serga, I. I. Syvorotka, F. Ciubotaru, C. Adelmann, B. Hillebrands, and A. V. Chumak, Appl. Phys. Lett. **110**, 152401 (2017).

[32] A. V. Chumak, A. A. Serga, and B. Hillebrands, Nat. Commun. **5**, 4700 (2014).

[33] C. S. Davies, A. V. Sadovnikov, S. V. Grishin, Y. P. Sharaevsky, S. A. Nikitov, and V. V. Kruglyak, IEEE Trans. Magn. **51**, 1 (2015).

[34] H. Yu, O. d'Allivy Kelly, V. Cros, R. Bernard, P. Bortolotti, A. Anane, F. Brandl, R. Huber, I. Stasinopoulos, and D. Grundler, Sci. Rep. **4**, 6848 (2014).

[35] Y. V. Khivintsev, Y. A. Filimonov, and S. A. Nikitov, Appl. Phys. Lett. **106**, 052407 (2015).

[36] M. Collet, O. Gladii, M. Evelt, V. Bessonov, L. Soumah, P. Bortolotti, S. O. Demokritov, Y. Henry, V. Cros, M. Bailleul *et al.*, Appl. Phys. Lett. **110**, 092408 (2017).

[37] A. Krysztofik, H. Głowiński, P. Kuswik, S. Zietek, L. E. Coy, J. N. Rychły, S. Jurga, T. W. Stobiecki, and J. Dubowik, J. Phys. D **50**, 235004 (2017).

[38] A. Talalaevskij, M. Decker, J. Stigloher, A. Mitra, H. S. Körner, O. Cespedes, C. H. Back, and B. J. Hickey, Phys. Rev. B **95**, 064409 (2017).

[39] S. Maendl, I. Stasinopoulos, and D. Grundler, Appl. Phys. Lett. **111**, 012403 (2017).

[40] J. Chen, F. Heimbach, T. Liu, H. Yu, C. Liu, H. Chang, T. Stückler, J. Hu, L. Zeng, Y. Zhang *et al.*, J. Magn. Magn. Mater. **450**, 3 (2018).

[41] H. Yu, O. d'Allivy Kelly, V. Cros, R. Bernard, P. Bortolotti, A. Anane, F. Brandl, F. Heimbach, and D. Grundler, Nat. Commun. **7**, 11255 (2016).

[42] C. Liu, J. Chen, T. Liu, F. Heimbach, H. Yu, Y. Xiao, J. Hu, M. Liu, H. Chang, T. Stueckler *et al.*, Nat. Commun. **9**, 738 (2018).

[43] S. Maendl and D. Grundler, Appl. Phys. Lett. **112**, 192410 (2018).

[44] H. Qin, S. J. Hämäläinen, and S. van Dijken, Sci. Rep. **8**, 5755 (2018).

[45] S. Klingler, V. Amin, S. Geprägs, K. Ganzhorn, H. Maier-Flaig, M. Althammer, H. Huebl, R. Gross, R. D. McMichael, M. D. Stiles *et al.*, Phys. Rev. Lett. **120**, 127201 (2018).

[46] Y. Krockenberger, H. Matsui, T. Hasegawa, M. Kawasaki, and Y. Tokura, Appl. Phys. Lett. **93**, 092505 (2008).

[47] R. Huber, Ph.D. thesis, Technische Universität München, 2013.

[48] T. Weiland, M. Timm, and I. Munteanu, IEEE Microwave Mag. **9**, 62 (2008).

[49] V. Vlaminck and M. Bailleul, Phys. Rev. B **81**, 014425 (2010).

[50] B. A. Kalinikos and A. N. Slavin, J. Phys. C **19**, 7013 (1986).

[51] M. Madami, S. Bonetti, G. Consolo, S. Tacchi, G. Carlotti, G. Gubbiotti, F. Mancoff, M. A. Yar, and J. Åkerman, Nat. Nanotechnol. **6**, 635 (2011).

[52] F. Ciubotaru, T. Devolder, M. Manfrini, C. Adelmann, and I. P. Radu, Appl. Phys. Lett. **109**, 012403 (2016).